Nucleation, Growth, Fractal Aggregation, and Late-Stage Coarsening on Structural Development of Polymer Physical Gels

Che-Min Chou and Po-Da Hong*

Department of Polymer Engineering, National Taiwan University of Science and Technology, Taipei 10673, Taiwan

Received April 1, 2004; Revised Manuscript Received May 28, 2004

ABSTRACT: By using the time-resolved small-angle light scattering (TRSALS) technique, we present the real-time measurement of the physical gelation process for a crystalline polymer. To investigate the growth kinetics, a complete picture of the gel structural formation should be differentiated into the nucleation and growth of the microgels, the diffusive aggregation of the microgels, the percolation in cluster−cluster aggregation process, and the late-stage coarsening by the Ostwald ripening process. We propose some phenomenological functions to describe the hierarchical structure of the nucleation gels. The modeling of the late-stage gel structure could be built upon the following three relevant categories: the structure of the primary particle, the nonfractal local structure of a random packing of the nearest neighbors, and the fractal correlations between the particles constituting the aggregates. The model is able to reproduce the overall behavior of H_v and V_v scattering intensity distributions over the experimental q range and holds the truth of the gel structural development in the late-stage coarsening process.

Introduction

Undeniably, the mechanisms of structural formation of polymer physical gels are very complex. The extremely subtle gelation phenomena still have not been fully elucidated. In studying the formation of gel structure, two interrelated subjects may be considered: (1) the formation of three-dimensional network structure; (2) the nature of network junction point in gel. The first subject pointed out that gelation is the phase transition (critical phenomena). The essential physical feature of a gel is its geometrical connections, and hence theoretical progress generally emphasizes percolation phenomena to gelation theory.[1−3] In addition to this, the community interested in polymer gels is the nature of network junctions. The junctions can be created by the permanent chemical cross-link or appropriate physical influences [i.e., first-order phase transition (crystallization and liquid−liquid phase separation), some specific molecular association (polar, complex, or colloid), or the result of entanglements].[4] In the present study, we confine our attention to the case of gels associated with phase transition (both percolation phenomena on the formation of three-dimensional network structure and first-order phase transition on the local junction-forming) and deserve explicit emphasis that the gelation is typically governed the coupling of several phase transitions.

Most studies of gelation behaviors have focused on phase behavior (the structure and thermal properties of the junction points by using neutron scattering, X-ray diffraction, DSC, etc.) and structural morphology (the equilibrium structure of the gels by using optical microscopy or SEM) in physical gels.[5,6] However, in this paper we will not follow the current trend. We would like to look at the gel structural development from a different angle, such as *the real-time observation* from the "mesoscopic (∼μm)" point of view. Thus, it is not necessary for the purpose of this paper to enter into a detailed discussion for the chemical structure of polymer chain, solvent type, molecular weight of polymer, lattice of polymer chains in a crystal, and degree of crystallinity. What we wish to show in this paper is how to illustrate a reasonable and clear phenomenological model especially on the structural formation of nucleation gel.

In our previous study,[7] we report the first real-time observation of crystal nucleation and concentration fluctuation during the physical gelation process of a crystalline polymer and prove that the spontaneous concentration fluctuation by spinodal decomposition is not a prerequisite for the formation of large-scale heterogeneous gels. In contrast with spinodal gels, now we call it nucleation gels. The present paper is a sequel to the previous paper. We show new and completed data on the time evolution of the V_v scattering and calculation in both the H_v and V_v scattering functions as well as a phenomenological model to describe hierarchical structure and late-stage coarsening of nucleation gels.

Experimental Section

Materials. The crystalline polymer used in this study is poly(vinylidene fluoride) (PVDF) powder ($M_w = 2.75 \times 10^5$ and $M_w/M_n = 2.57$, Aldrich Chem. Co.). The solvent was a mixture of tetra(ethylene glycol) dimethyl ether (TG) and $LiCF_3SO_3$ salt. The salt was added to give an O:Li ratio (oxygen atoms in the TG:lithium atoms in the salt) of 12:1. The polymer gel electrolytes were prepared by quenching 4 g dL^{-1} homogeneous PVDF solution from 433 K to the gelation temperature 303 K.

Probing Structure by TRSALS. Small-angle light scattering is one of the most useful real-time techniques to study mesoscopic disordered systems that present inhomogeneities on length scales at the order of the wavelength of light or larger.[8−13] However, most of the light scattering measurements in aggregation systems were concentrated on polarized (V_v scattering) or unpolarized conditions, while the depolarized condition (H_v scattering) gave a treatment only for simply structural models (i.e., growth or deformation of polymer spherulites,[14] anisotropic rod,[15] and interspherulitic interference in the relative dilution limit). In the work, we would try to expand the depolarized scattering technique into an ag-

* Corresponding author: Fax +886-2-27376544; e-mail poda@mail.ntust.edu.tw.

10.1021/ma049361f CCC: $27.50
Published on Web 07/02/2004

gregation system and first combine H_v with V_v scattering to interpret the complicated structural development of the polymer physical gels.

The optical arrangement of the TRSALS apparatus has been described previously.[7] A plane-polarized laser beam (5 mW He−Ne laser having a wavelength of 632.8 nm) was used as the incident source, and the polarization direction of the beam was varied by a half-wave plate. The sample cell was placed on TMS-600 heating stage (Linkam Scientific Co.), and the scattered light intensity of the sample was directly imaged through a Fourier lens and an analyzer onto the CCD camera (Apogee Instruments Inc., AP 7p with a 512 × 512 pixel sensor). The digitized images were transferred the real-time processing to a personal computer. In our design the angular range for which reliable data can be collected is about θ = 0.5°−20°, corresponding to $q = 0.124-4.942\ \mu m^{-1}$ and length scale 1.27−50 μm [$q = (4\pi m_1/\lambda)\sin(\theta/2)$, where q is the scattering vector, λ is the wavelength of incident light, and m_1 is the refractive index of an isotropic medium].

Gelation Time. The test tube tilting method was used to determine the gelation time t_{gel}, which was defined by observing cessation of liquid flow inside the test tube when it was tilted, and the gelation time was monitored just after the test tube was put into the thermostatic bath.

Results and Discussion

Scattering Patterns of the Nucleation Gels. Figure 1 shows a series of H_v (left) and V_v (right) scattering patterns during isothermal gelation. It is interesting that the time changes in the shape of the present H_v patterns can be divided into three stages: (1) a four-leaf-clover pattern in early stage (see Figure 1a−c); (2) a four-crescent-moon pattern in medium stage (see Figure 1d); (3) a double structure in final stage (see Figure 1e,f), which includes both four-leaf-clover and four-crescent-moon shapes at low and high angle range, respectively. In contrast to the complicated H_v scattering, we see only a monotonic decay of the scattering intensity with θ and a nearly circularly symmetrical V_v scattering pattern. Simultaneously, the time changes in the present V_v patterns are also unexciting except for the striking increase with concentration of the intensity distribution on the center of the pattern. The similar scattering patterns have been observed in our previous paper for 6 g dL^{-1} PVDF gels.[7] We have pointed out that the initial pattern with the four-leaf-clover shape implies the growth of the optically anisotropic spheres, and the conversion of the pattern from the four-leaf-clover to the four-crescent-moon shape with the emergence of new first-order peak is the main characteristic of the anisotropic-to-isotropic transition. In terms of the birefringent transition, it seems reasonable to suppose that the origins of the patterns in Figure 1 are produced by aggregation of isotropic spheres. However, we should not overlook that the crystallite act as the major junctions in the gel networks.[7,16,17] We miss the point if we regard the complicated pattern evolution merely as the birefringent transition of the spheres. Thus, there is room for argument on these points, and below we would propose a more precise account of these problems.

To clarify this issue at once, we show how the birefringence of the sphere affects the H_v and V_v scattering patterns. A series of the H_v (top) and V_v (bottom) scattering patterns calculated from eqs A5−A9 are shown in Figure 2a by taking the sphere radius a_0 as 4 μm, the relative index μ as 0.993, and the refractive index of the medium m_1 as 1.433 (see Appendix A). For the sake of qualitative discussion, the scattered intensity distributions of the calculated pattern were shown by arbitrary units. The extreme left patterns ($\Delta\mu$ = 1) are for a polymer spherulite (a strongly birefringent sphere) and show the typical four-leaf-clover H_v pattern with the 2-fold symmetrical V_v pattern. These patterns correspond to what would be predicted by SR theory.[14] The extreme right patterns ($\Delta\mu$ = 0) corresponds to the light scattering by a amorphous sphere (a optically isotropic sphere). For H_v scattering, we see a first-order peak with the four-leaf-cover shape at the center of the pattern, superimposed

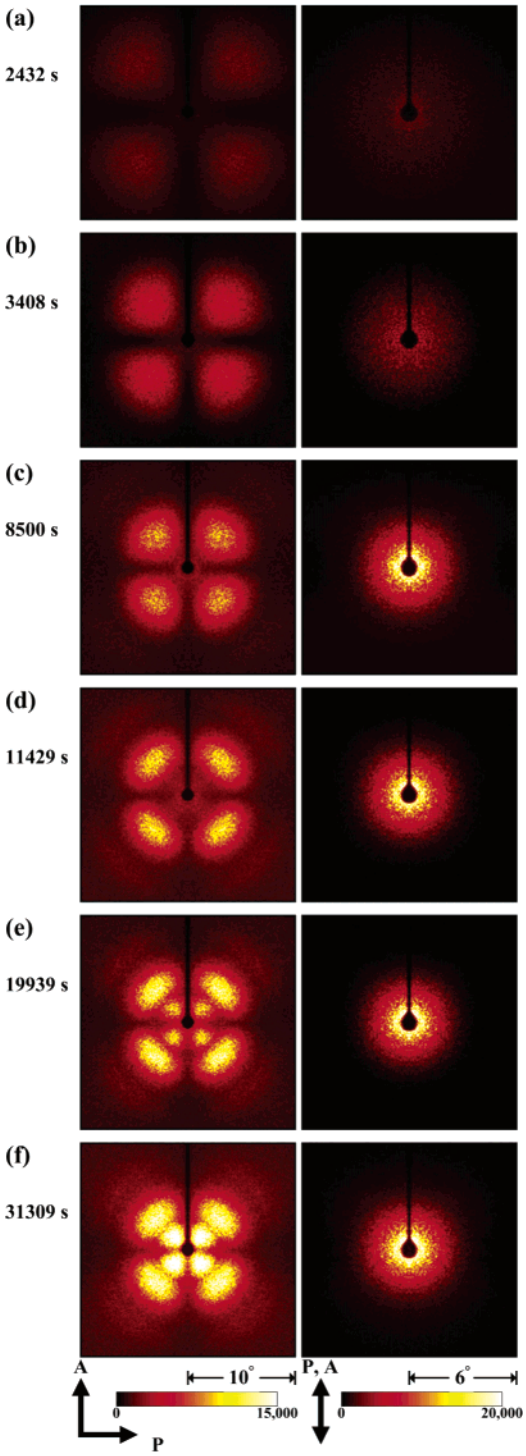

Figure 1. Time evolution of H_v (left) and V_v (right) scattering patterns showing the isothermal gelation for 4 g dL^{-1} PVDF-TG-LiCF$_3$SO$_3$ solution at 303 K.

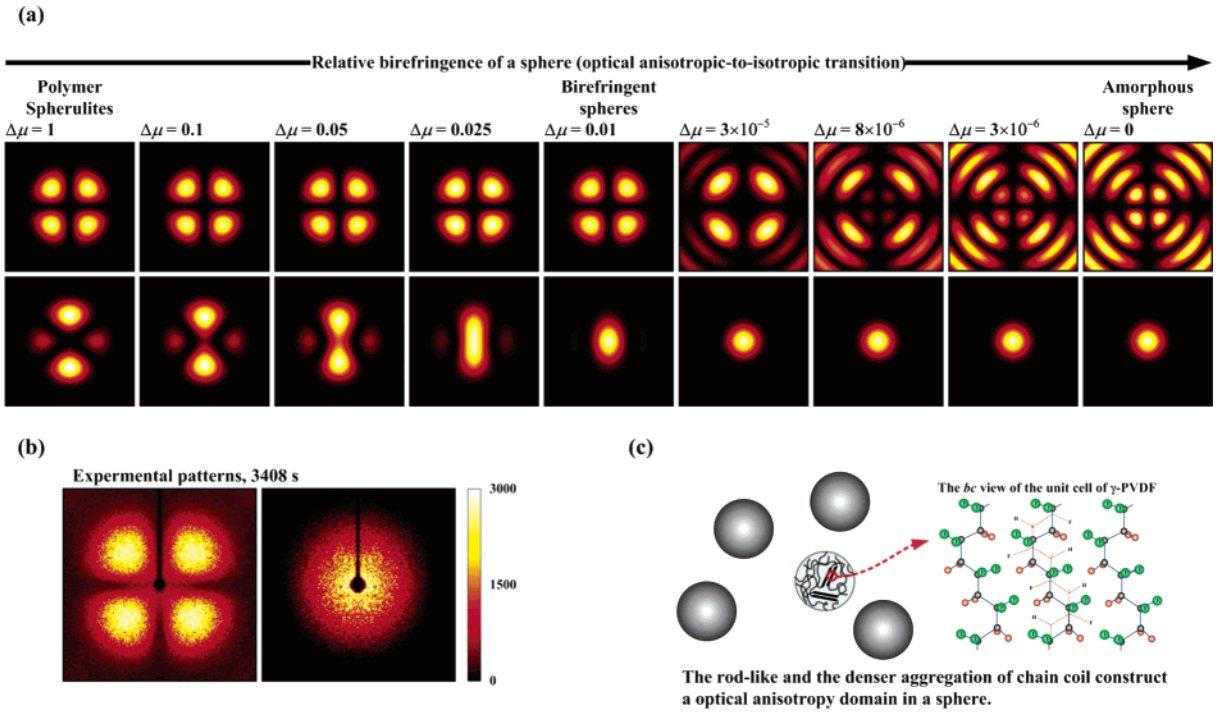

Figure 2. (a) Calculated H_v (top) and V_v (bottom) scattering patterns for a birefringent sphere as a function of the relative birefringence $\Delta\mu$. The sphere radius is 4 μm, the relative index $\mu = 0.993$, the refractive index of the medium $m_1 = 1.433$, and the scattering angle $\theta = 10°$. (b) Experimental scattering patterns at sol state. (c) Schematic representation of the birefringent sphere.

on many higher-order peaks with the four-crescent-moon shape. On the other hand, we see only a circularly symmetrical V_v scattering pattern. As seen in the figure, when the birefringence of the sphere is decreased, the changes in the shape of the H_v and V_v scattering pattern are observed. Figure 2b shows the experiential scattering patterns taken at 3408 s in the sol state. The first point to notice is that the experiential scattering patterns in Figure 2b look the same as the calculated scattering patterns for the birefrigent sphere (the middle patterns, $\Delta\mu = 0.01$). Thus, there is no disagreement on the point that the H_v and V_v scattering give the conclusive evidence for the aggregation of birefringent spheres in the present gel system. We can imagine that crystallites or fibrils act as junction points for the intermolecular cross-linking within the polymer-rich droplets, leading to the formation of the microgels and approximate dispersion of the hard spheres in the solution. The schematic representation of the birefringent sphere (or rather the microgel) is shown in Figure 2c. Let us now return to the main: whether we can regard the complicated pattern evolution shown in Figure 1 as the birefringent transition of the spheres or not.

Figure 3a shows the three-dimensional map-surface plots of the experimental H_v scattering patterns taken at 31 309 s (gel state) and (b) the calculated one for $\Delta\mu = 0$. We are confronted by two difficulties. The first is that the theoretical prediction of sharp higher-order peaks as shown in Figure 3b is not observed in the experimental H_v scattering patterns. The second is that the experimental intensity ratio of first to second scattering order (see Figure 3a) is much larger than the theoretical prediction of an isotropic sphere (see Figure 3b). The complicated pattern evolution, as we have seen, is not quite as simple as previously suggested. However, looking briefly at the time evolution of scattering profiles may help us to account for the origins of these patterns.

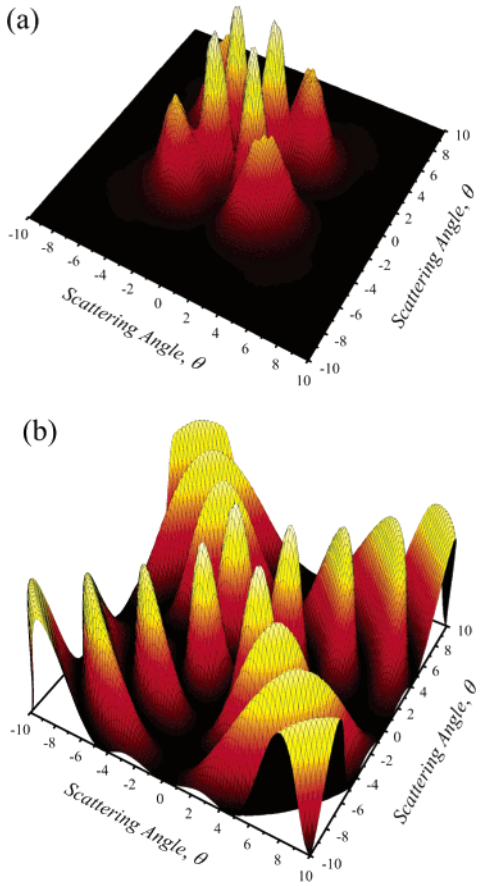

Figure 3. Three-dimensional map surface plots of the H_v scattering patterns: (a) experimental pattern at 31 309 s; (b) the calculated pattern for a amorphous sphere [the parameters are the same as in Figure 2a for $\Delta\mu = 0$].

Time Evolution of the Scattering Profiles. Figure 4 shows the time-resolved H_v scattering profiles at $\varphi =$

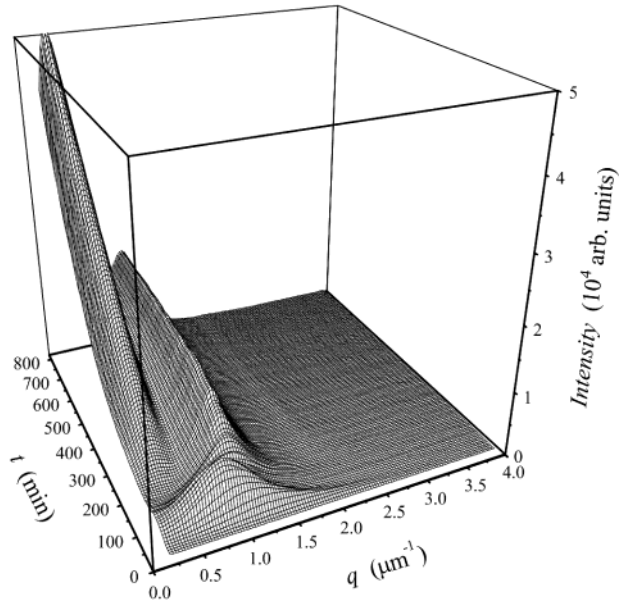

Figure 4. Time evolution of H_v scattering profile at $\varphi = 45°$ a for 4 g dL^{-1} solution after a temperature jump from 433 to 303 K.

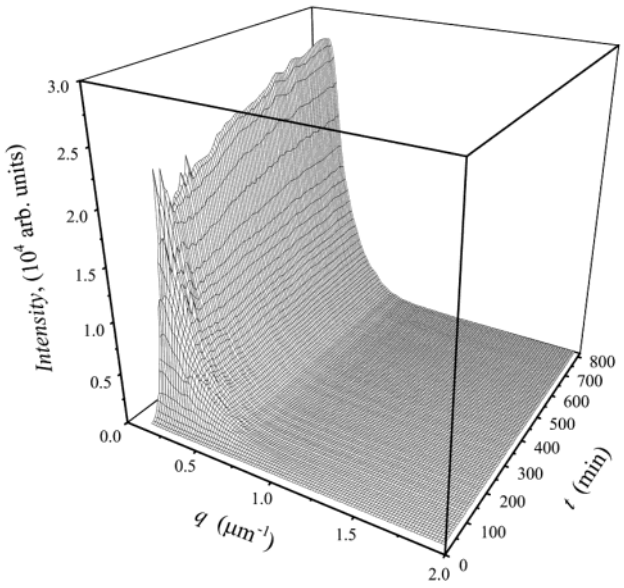

Figure 5. Time evolution of V_v scattering profile at $\varphi = 45°$ for a 4 g dL^{-1} solution after a temperature jump from 433 to 303 K.

45°. The first point to notice is that the peak intensity gradually rises, and the peak position shifts toward a smaller q range in early stage (t < 140 min). Following by this peak growth stage, we observe a counterintuitive process with the reverse growth of the peak position and a decrease in its intensity. At the same time, this process accompanies by conversion of the H_v scattering pattern from a four-leaf clover to a four-crescent-moon shape (see Figure 1a−d). Our previous paper grouped above two processes together as the initial stage of gelation (i.e., sol stage).[7] In this stage, the nucleation process of birefringent sphere is governed by the coupling of the local concentration fluctuation and polymer crystallization. Given that the nuclei growth in early stage is sufficiently isolated and exists the inhomogeneous density distribution of crystallites within the sphere (also called internal disorder[18]), we may attribute the counterintuitive process with conversion of the shape of the H_v scattering pattern to the slightly decreased birefringence of the sphere. We do not want to go into the minor details at the moment. However, we would like to particularly emphasize that the contribution of the internal disorder to decrease in the birefringence of the spheres is limited. Phenomenologically speaking, the view of the birefringent transition from an anisotropic sphere to a completely isotropic during the gelation process is unsatisfactory. The experimental results (see Figure 3) also support this view.

On the other hand, in late stage of gelation (t > 140 min, i.e., gel stage), the time-resolved H_v scattering profiles yield two peaks with different length scales. We identify the two different peak-growth modes: a steady-state mode, following by the initial peak in sol stage (t < 140 min), and a fast mode, a new first-order peak with a steep rise in its intensity. In contrast to the complex peak-growth behavior of the H_v scattering, Figure 5 shows the time-resolved V_v scattering profiles at φ = 45°. As the nuclei grow, the $I_{V_v,q}$~0 value, evaluated at the beam stop limit $q = 0.132\ \mu m^{-1}$, steeply rises to the peak about 120 min, the beginning of the counterintuitive process obtained from H_v scattering (Figure 4).

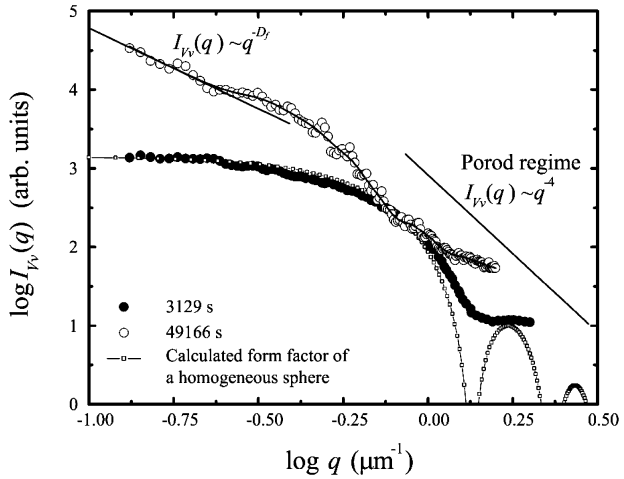

Figure 6. Plot of log $I_{V_v}(q)$ against log q obtained from the two time regimes: "sol" stage (t = 3129 s) and "gel" stage (t = 49 166 s). The calculated form factor for a homogeneous sphere represents the best theoretical fits for the experimental points in sol stage. The sphere form factor is calculated with $a = 3.35$ μm, $\mu = 0.993$, $\Delta\mu = 4 \times 10^{-4}$, and $m_1 = 1.433$.

After a marked increase in intensity, it indicates a nucleation and growth process, the $I_{V_v,q} \sim 0$ shows a slight rise.

Figure 6 shows examples of the double-logarithmic plot of $I_{V_v}(q)$ vs q for both sol and gel state. In the sol state (t = 3129 s), the figure shows the typical V_v scattering intensity distribution fitting with the calculated form factor for a homogeneous sphere by using eqs A5, A7, and A8. The form factor was calculated with $a_0 = 3.35\ \mu$m, $\mu = 0.993$, $\Delta\mu = 4 \times 10^{-4}$, and $m_1 = 1.433$. The parameters a_0, μ, and $\Delta\mu$ have been adjusted in order to get the best fit between the calculated form factor and the experimental data. The result also implicates that no interparticle aggregation was observed at least in the nucleation and growth stage. However, the essential physical feature of the gels is its geometrical connections. The V_v scattering from gel stage should provide a starting point to explain this singular gelation behavior.

Fractal Nature of the Gel Structure. The structure of aggregates and gels is highly disordered, and it can be described in terms of statistically scale invariant. The self-similar clusters are well described by the relation[19−21]

$$N = k_0(R_g/a_0)^{D_f} \quad (1)$$

where N is the number of primary particles or monomers in the aggregate, k_0 is the constant, R_g is the radius of gyration of the aggregate, a_0 is the particle radius, and D_f is the fractal dimension. According to the sticking probability, two limiting regimes of the aggregation process have been identified, namely, diffusion-limited cluster−cluster aggregation (DLCA) with $D_f \simeq 1.75$ and reaction-limited cluster−cluster aggregation (RLCA) with $D_f \simeq 2.1$.[22] The structural formation of the nucleation gels may be considered as a direct consequence of the fractal aggregation of the isolated microgels. A more general procedure for describing the fractal morphology of an aggregate is use of the notion of the spatial density−density correlation function $\langle\delta\phi(0)\delta\phi(\mathbf{r})\rangle$.[23] The overall density−density correlation function of an aggregate can be expressed as the convolution of the single-particle correlation function and the pair-correlation function. As usual, the scattered intensity $I(q)$ from such aggregate can be written as[24]

$$I(q) \sim P(q)\, S(q) \quad (2)$$

where $P(q)$ is the form factor, i.e., the scattering intensity for a spherical particle alone, and $S(q)$ is the structure factor, i.e., the spatial arrangement of the particles within an aggregate. Here $P(q)$ is directly related to the shape and the scattered ability of the particle, and it can be expressed by eqs A5 and A6. The structure factor displays a scaling behavior for $qa_0 \ll 1 \ll qR_g$ as $S(q) \sim q^{-D_f}$. This result is often used to determine the fractal dimension of a fractal object. As seen in Figure 6, in the gel stage ($t = 49\ 166$ s), the data clearly show a power law behavior at small q region, i.e., $I_{V_v}(q) \sim q^{-D_f}$, reflecting the fractal correlation of the microgels, while at high q region, the q^{-4} Porod behavior with weak oscillation is characterized by the form factor of the individual microgel.[25−27]

Growth Kinetics. To investigate the growth kinetics, the quantitative analysis of the data of H_v and V_v scattering is reported in Figure 7. The first point to notice is that the growth of the fractal dimension shows two different characteristic time regions, as shown in Figure 7a. There is a marked increase in the D_f value from ~1 to 1.75, the value of the DLCA model, and this increase slows down at the time across the macroscopic gelation, t_{gel}. At longer time, the D_f value slowly rises continuously until it is close to 2.1, the value of the RLCA model. Strictly speaking, the fractal description and its power law form (eq 1) are valid only in a statistical sense and reveal a greater deviation for the small clusters. However, a series of three-dimensional simulations of fractal-like clusters, containing limited numbers of primary particles per cluster, were carried out by Yang and Biswas, and the statistical averaging over a large number of clusters revealed that average fractal dimension decreases as the cluster size decreases.[28] Thus, the marked increase in the D_f value can be attributed to the growth of cluster size during the fractal aggregation of the microgels. As time elapses, when the number of the particles is present above a critical volume fraction, the cluster−cluster aggregation processes will lead to form a space spanning structure and gelation occurs. On the other hand, for each measurement of the H_v intensity distribution, we determined the peak intensity I_m and the corresponding characteristic wave vector q_m, as shown in Figure 7b. Comparing the scattering results with the gelation time, some distinct features can be seen. The gel structural formation consists of four major stages: (1) an nucleation and growth in regime I, (2) a fractal aggregation of the microgels in regime II, (3) a percolation in cluster−cluster aggregation process in regime III, and (4) a ripening process in regime IV.

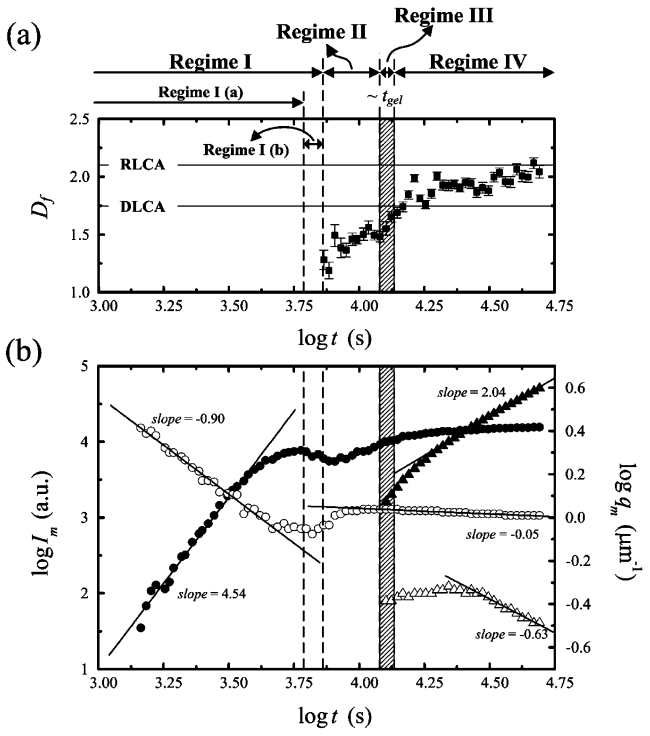

Figure 7. (a) Time evolutions of the D_f obtained from $I_{V_v}(q)$ decays as a power law function, $I_{V_v}(q) \sim q^{-D_f}$ at low q regime as reported in Figure 6. (b) Gelation study by the H_v scattered condition. The left abscissa corresponds to the peak intensity I_m ($I_{m,I}$, solid circle; $I_{m,II}$, solid triangle) while the right one gives the characteristic wave vector q_m ($q_{m,I}$, open circle; $q_{m,II}$, open triangle) as a function of time after a temperature jump.

In early stage of the nucleation and growth [regime I (a)], both I_m and q_m values exhibit nearly power-law growth behavior with time ($I_m \sim t^{\beta}$, $q_m \sim t^{-\alpha}$: $\alpha = 0.90$, $\beta = 4.54$). In late stage of the nuclei growth [regime I (b)], we observed a counterintuitive process, attributed to the inhomogeneous density distribution of crystallites within the microgels. We have already discussed these behaviors fully in either the preceding section or our previous paper[7] and may leave the details to the complicated aggregation behavior. In the nucleation and growth stage, the following picture is widely accepted. The nuclei grow by simple accretion from the oversaturated surrounding solute by downhill diffusion, having a positive diffusion coefficient. We may reasonably expect that the nuclei growth will be stopped when the process exhausts the resources of the oversaturated solute in surroundings. Thus, the cluster−cluster diffusive aggregation will be relieved as a main process to dominate the structural development (see regime II). When the gel point is approached, a strong overlap between the fractal-like clusters with the percolation

in cluster−cluster aggregation process will be observed as shown in regime III. Conceptually, the fractal-like clusters growth close to the gel point can be described in terms of bond percolation models.[24] We may consider a simple picture that the centers of fractal-like clusters occupy all sites of a three-dimensional periodic lattice, and then each bond between the close-packed fractal-like clusters is formed randomly with probability. The point we wish to emphasize here is that the percolation transition has a characteristic of critical point in the physical sense. However, the measuring t_{gel} clearly reveals the existence of a wide time region. We may tentatively refer the broadening of the percolation transition to the size distribution effect of polydisperse fractal aggregates.

In late stage of gelation ($t > t_{gel}$), it would be expected that the structural development behavior is restrained by the macroscopic gelation. But it is interesting to note that the regime IV shows excessively complicated structural development behavior. We see a slow rise in D_f (Figure 7a), two different peak growth modes (Figure 7b), and the complicated H_v scattering patterns (Figure 1e,f). We can safely state that the new nuclei or some new structure is unlikely to appear in this stage. On the other hand, to regard the excessively complicated structural development behavior merely as arrangement or growth of microstructure such as crystallites or fibrils texture within the microgels is also unsatisfactory. The most likely explanation for the behavior in regime IV is that some ripening processes accompanied by the restructuring of the fractal-like clusters occur in late stage of gelation process. In next section, our concern is to consider what a reasonable model and the corresponding structural characteristics for the nucleation gels are.

Modeling of Late-Stage Gel Structure. A more fundamental picture of the gel structure in late-stage ripening processes should be built upon the explicit assumption of four relevant categories: the structure of the primary particle (the microgel), the nonfractal local structure of the nearest neighbors, the short-range fractal correlations, and the long-range intercluster correlations. As q range is limited, the long-range intercluster correlations could not be discussed here. Thus, we can substantially simplify the complexity of the model. We would propose some phenomenological functions to describe the hierarchical model of the nucleation gels. In the preceding section we pointed out that the structure of the microgel can be quantified through the single particle form factor (see Appendix A). For the present, we shall confine our attention to the specific form of the nonfractal local structure and the structure of the fractal aggregates. The gelation is considered as a direct consequence of the growth of fractal aggregates (see Appendix B). The general behavior of the $S(q)$ can be classified into the following regions: $q\xi \leq 1$ (Guinier region, where the R_g of the aggregates can be determined using the Guinier plot), $1/\xi < q < 1/a_0$ (fractal region), and $qa_0 > 1$ (asymptotic region, where $S(q) \simeq 1$ and one sees only the scattering due to the individual particles).

In addition to the fractal correlations, it is interesting to note the nonfractal local structure of the nearest neighbors within an aggregate. We can say with fair certainty that the nonfractal local structure acts an important role in determining the physical properties of the ultimate structure of the gels. To further investigate the effects of the nonfractal local structure on the $S(q)$, Hasmy et al.[26] showed that the general behavior of the nonfractal local structure (i.e., the particles are arranged as in a random packing of the hard spheres) can be explained in terms of the center-to-center interparticle distance distribution function with Fourier transform $S_\infty(q) \sim 1 + z \sin x/x$ (where z is the coordination number of nearest neighbors for each particle and $x = 2qa_0$). As expected, $S_\infty(q)$ exhibits a broad minimum followed by a damped oscillation at the high q region ($qa_0 > \pi$). The oscillations can be attributed to the presence of nearest neighbors in the hard-sphere contact with the particle at the origin. We may expect that the concept of the oscillation function introduced above helps account for the underlying origins of the complicated H_v scattering behavior in regime IV. However, because of the strong disorder and the particle size polydispersity in the present system, these oscillations are highly damped and can be ignored. In addition to this, from the structural development point of view, since the hard-sphere packing effect was fixed by the early stage of the aggregation process (regime II), it could not account for the excessively complicated structural development behavior observed in regime IV. Thus, we need a new oscillation function to explain the dynamics of the local structural development in late-stage gelation.

The first question to be discussed is what the phenomenological difference between the microgels growth in regime I and the ripening in regime IV is. Most of us would accept that in regime I the microgels grow by the simple accretion from the oversaturated surrounding solute. However, this process does not be observed in regime IV. In contrast to our system, a wide variety of other systems present the same features in late-stage of the aggregation, growth, or coarsening.[29−32] These phenomena are driven by the system trying to minimize its interfacial free energy, resulting in an increase of the average domain size and a decrease of the total number of droplets. In principle, two different processes have been used to describe the droplet growth in late stage. The first, known as Ostwald ripening, is attributed to Lifshitz and Slyozov[33] and Wagner,[34] who considered the noninteracting limit with the volume fraction $\phi \rightarrow 0$ for the immobile droplets. According to this model, the mass transport between the stationary droplets is governed by a thermodynamic driving force (i.e., the chemical potential of a droplet is proportional to its radius of curvature; thus, the molecules detach/evaporate from a small, high-curvature droplet and diffuse/condense onto another large, low-curvature droplet in the vicinity).[29,30] The second model considered the coarsening via dynamic coalescence of the diffusing droplets.[31,32] In this model, the droplets undergo random Brownian motion, and growth occurs when two droplets accidentally collide and coalesce to increase the mean droplet size. Recalling our earlier discussion, the gelation process can be governed by the hard-sphere-like colloid aggregation, and the cluster diffusion is restrained by the macroscopic gelation. We can say that the liquidlike coalescence between two droplets is not observed in the present system. Thus, Ostwald ripening clearly appears to be a better model than dynamic coalescence for interpreting the structural development in regime IV. This feature of late-stage ripening is schematically illustrated in Figure 8a. Let us consider the following processes. The hard-sphere-like microgels

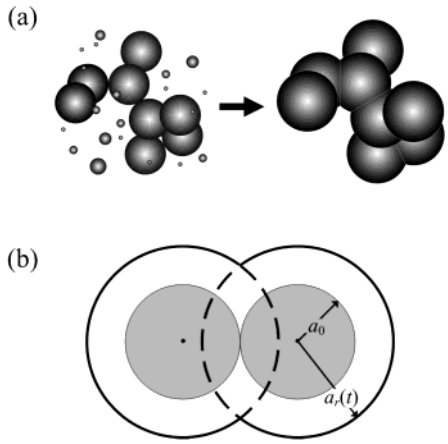

Figure 8. (a) Sketch of the late-stage coarsening model. (b) Schematic representation of the two interpenetrated spheres.

aggregate to form fractal clusters, which ultimately constitute a three-dimensional network structure. Because of the broad particle size distribution and the hard-sphere contact in system (i.e., high specific surface area), the system tries to minimize its interfacial free energy by Ostwald ripening. Therefore, the mass transport takes place via polymer dissolution from small particles and reprecipitation in the surface of backbone of the gel network or in the necks between the particles. Besides reducing the interfacial free energy, this process is also accompanied by a stiffening of the weak network structure.

Modeling of the scattering function using the actual structure of the gels is too complicated. In view of this, a simple model is developed to account quantitatively for the local structural feature and the kinetic late-stage ripening process. In this model only the relationship between the two particle hard-sphere contacts has been considered, and the coarsening of the two contact spheres of a size a_0 is shown in Figure 8b. A sphere doublet is formed by Ostwald ripening process, and the growth of the sphere doublet can be characterized by a single time-dependent length parameter $a_r(t)$. Here, we were first to decouple the effects of the nonfractal local structure away from the general expression of the $S(q)$ to the $P(q)$ and then calculate the $P(q)$ of the two interpenetrated spheres (see Appendix C).

As described above, the hierarchical model of the nucleation gels can be built upon the explicit assumption of four relevant categories. After several trials, we propose some phenomenological functions which are

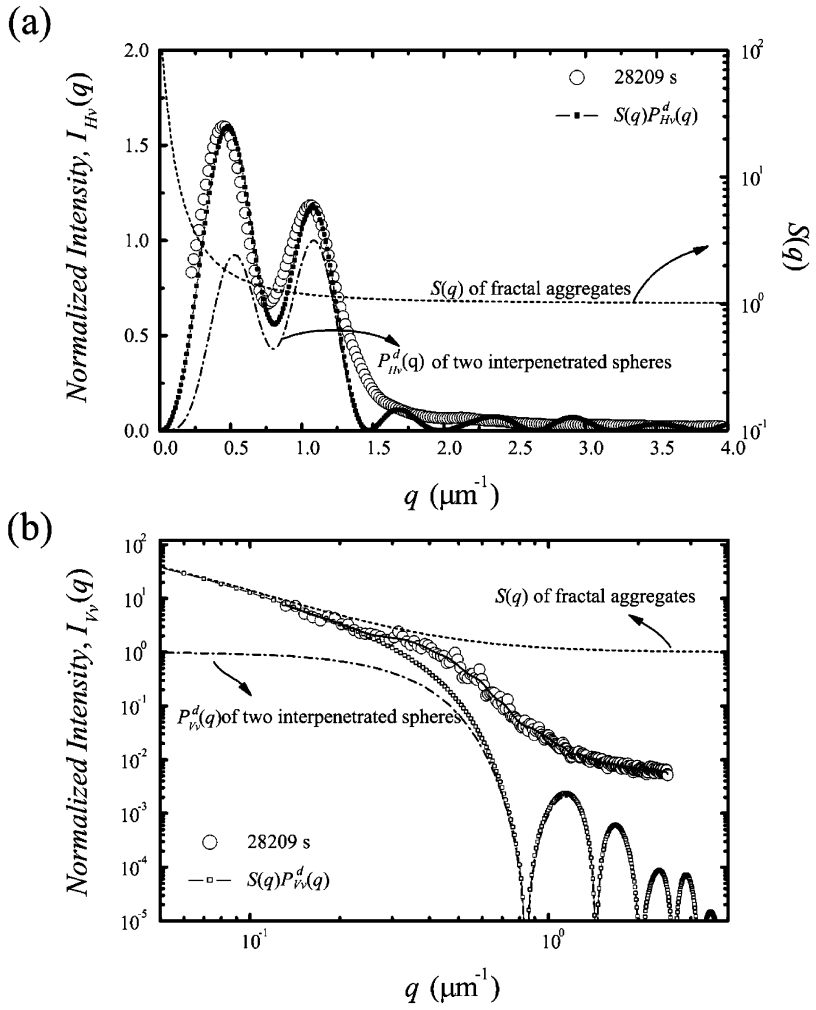

Figure 9. Behavior of the normalized scattered intensity distribution obtained from the experimental points in gel stage (φ = 45°) as a function of the wave vector q (open circle). The dashed line corresponds to the structure factor of the fractal aggregates $S(q)$ (eq B2) for a single aggregate containing 200 particles (a_0 = 3.4 μm) and the fractal dimension D_f = 1.86. The dash−dotted line corresponds to the form factor of the two interpenetrated spheres (Ostwald ripening) [$P^d_{V_v}(q)$: eq C3; $P^d_{H_v}(q)$: eq C4] for the overlapping parameter F = 0.64 (a_r = 5.34 μm), μ = 0.993, $\Delta\mu = 6.9 \times 10^{-5}$, and m_1 = 1.433. The product of $S(q)$ and $P(q)$ represents the best theoretical fits for the experimental points in the gel stage. (a) H_v scattered condition. (b) V_v scattered condition.

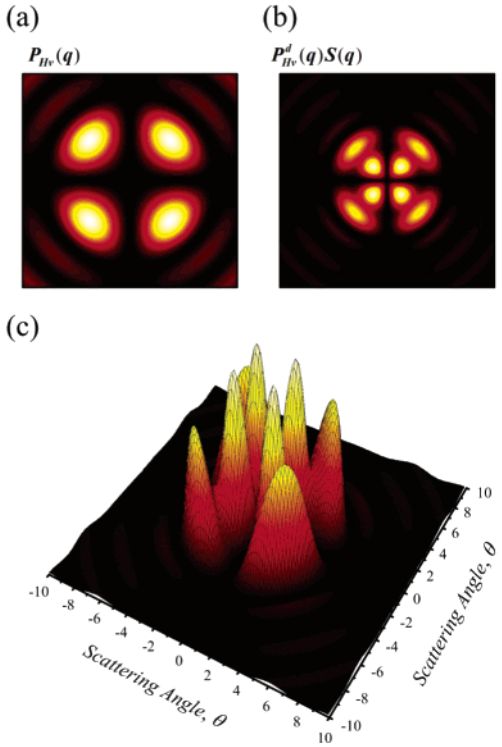

Figure 10. Calculated H_v scattering pattern for a sphere (a). Calculated H_v scattering pattern (b) and the corresponding three-dimensional map surface plot (c) for a model of the Ostward ripening in colloidal gels. The parameters are the same as in Figure 9.

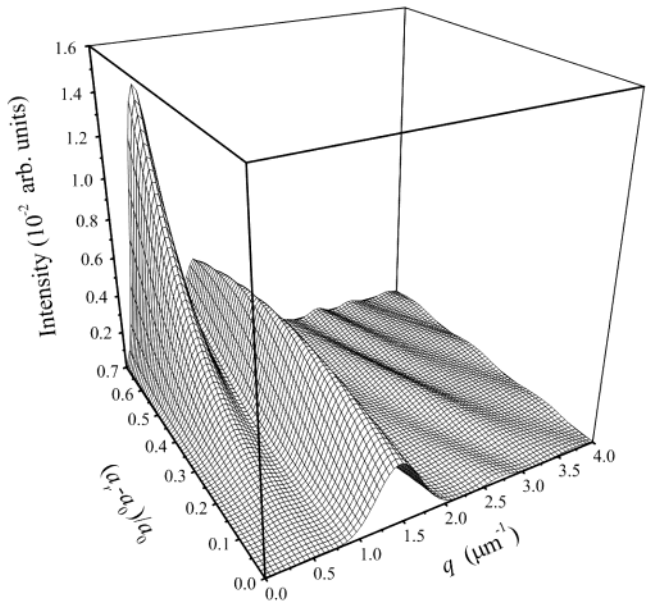

Figure 11. Calculated H_v scattering profile at $\varphi = 45°$ during the structure evolutions in the late-stage coarsening for Ostward ripening. The parameters are the same as in Figure 9.

able to reproduce the overall behavior of H_v and V_v scattering data over the experimental q range. Figure 9 shows the comparison of the experimental normalized scattered intensity distribution with the calculated one by eqs 2, B2, C3, and C4 in regime IV. Our full model is described by six parameters: a_0, μ, $\Delta\mu$, F, D_f, and N. Each of best-fit parameter values is shown in the caption. It is interesting to note that for the gels studied in the present work the experimental q range was located within the crossover between the fractal and the Porod regime. Since the crossover between fractal and long-range intercluster correlations could not be observed, the number of primary particles in an aggregate was determined by supposition, and this value is insensitive in the present q range. We may note, in passing, that, in contrast to the V_v scattering, the H_v scattering is more sensitive to the local structural feature of the aggregates. Similarly, the calculated H_v scattering pattern for our phenomenological model is given in Figure 10. In contrast to the calculated H_v scattering pattern for a sphere (Figure 10a and calculated by eq A6), the calculated H_v scattering pattern (Figure 10b) with the corresponding three-dimensional map surface plot (Figure 10c) for our proposed model clearly shows the double structure, and the calculated results almost agree with the experimental one (see Figure 1f). More noteworthy is that the model holds the truth of the gel structural development in late-stage ripening processes. It seems reasonable to conclude that the slow rise in D_f value of regime IV can be regarded as a consequence of late-stage ripening. Earlier in this paper, we left the problem of two different kinetic growth modes untouched. At present, the excessively complicated structural development behavior observed in regime IV (see Figure 4) is successfully reproduced in Figure 11. We see that the emergence and the steep growth of new first-order peak are the main characteristics of the coarsening process, and the two kinetic growth modes can be characterized by a single time-dependent length parameter $a_r(t)$. In view of this, maybe we can consider how to expand this argument into the scaling behavior of structure and growth kinetics, the universal features in late-stage aggregation, growth, and coarsening. We leave the matter open, and it will be taken up in our next study.

Conclusion

In this work, we report the real-time observation of the structural development of the nucleation gels. It is clear that the experimental results are entirely different from the general concept of the "spinodal gels" and also imply that the spontaneous concentration fluctuation by spinodal decomposition is not a prerequisite for the formation of the large-scale heterogeneous gels. In particular, we propose some phenomenological functions which are able to reproduce the overall behavior of H_v and V_v scattering over the experimental q range and hold the truth of the gel structural development in the late-stage coarsening process of the nucleation gels.

To investigate the growth kinetics, a complete picture of the gel structural formation is schematically shown in Figure 12. When an oversaturated crystalline-polymer solution is quenched from high-temperature disordered phase into a two-phase or multiphase metastable region, governed by the coupling of the crystal and concentration order parameters, the microgels is formed by the process of nucleation and growth. We can imagine that the crystallites or the fibrils act as junction points in the microgels, leading to approximate dispersion of the hard spheres in the solutions [regime I (a)]. In the late-stage nuclei growth [regime I (b)], a unique feature of the birefringent transition of the microgels can be attributed to the inhomogeneous density distribution of crystallites within the microgels. We can reasonable expect that the nuclei growth would be stopped when the process exhausts the resources of the

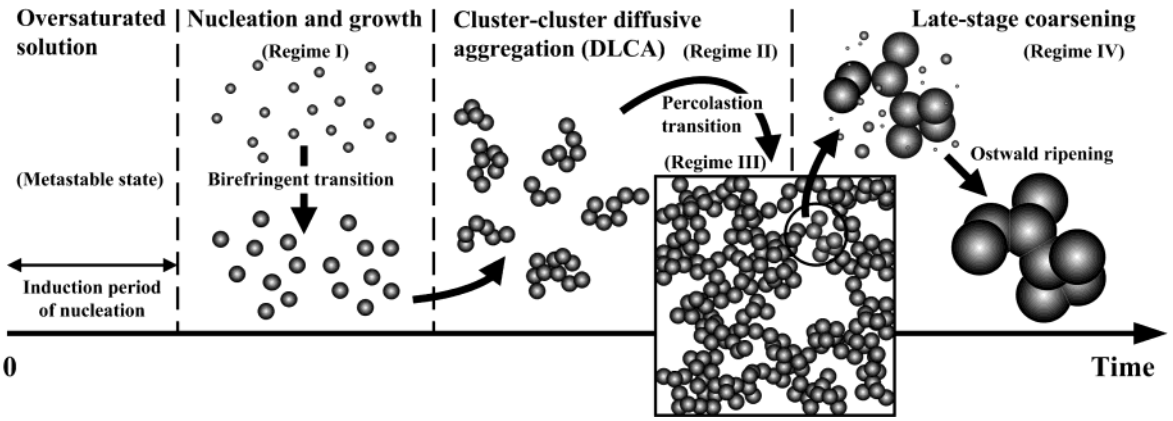

Figure 12. Schematic representation of the structural formation of the nucleation gels.

oversaturated solute in surroundings. The cluster−cluster diffusive aggregation would be relieved as a main process to dominate the structural development (regime II). When gel point is approached, a strong overlap between the fractal-like clusters with the percolation in cluster−cluster aggregation process would be observed (regime III). In late stage gelation (regime IV), the system tries to minimize its interfacial free energy by the coarsening process. The mass transport takes place via polymer dissolution from small particles and reprecipitation in the surface of the backbone of the gel network or in the necks between the particles. At the same time, this process is also accompanied by a stiffening of the weak network structure. The point we wish to emphasize is that the nonfractal local structure acts an important role in determining the physical properties of the ultimate structure of the gels.

In conclusion, we can expand the structural formation of the nucleation gels into two individual topics: the first is how to illustrate a reasonable phenomenological model on the nucleation gels and the second is what the thermodynamic essences and the corresponding kinetics of the early-stage nucleation are (i.e., the coupling of the local concentration fluctuation and the polymer crystallization). Having got the structural model of the nucleation gels amply established, we will shift the emphasis away from structural morphology to the phase behaviors. The thermodynamic essences and the corresponding kinetics of the early-stage nucleation are little understood. The questions of the coupling behavior of the concentration and the crystal order parameter should be explained appealing to either the thermodynamic concept of the "spinodal nucleation",[35] where is the non-mean-field-like behavior of the first-order phase transition, or the kinetics concept of the "spinodal-assisted crystallization",[8,36] where the conformation−density (or concentration) coupling can induce a liquid−liquid phase separation. Having made this distinction, we will begin with a simple observation. TRSALS is one of the most useful techniques to study the early-stage fluctuation and phase behavior in two-phase or multiphase system. We need not elaborate on this point; it is treated much more adequately in our next work.

Acknowledgment. The authors thank the National Science Council of the Taiwan for financially supporting this research under Contract NSC-92-2216-E-011-018.

Appendix A

The problem of light scattering from a particle can be described by the particle's scattering matrix[37]

$$\mathbf{S} = \begin{bmatrix} S_2 & S_3 \\ S_4 & S_1 \end{bmatrix} \tag{A1}$$

where S_1, S_2, S_3, and S_4 are the four amplitude functions. All information about the bulk optical properties and the physical structure of the scatterer are contained in the matrix. In general, we can regard the scattering matrix as a certain optical component such as polarizer and analyzer. A complete description of scattering theory is to relate the electric vectors of the scattered light $\{\mathbf{E}_l, \mathbf{E}_r\}$ to the incident light $\{\mathbf{E}_{l_0}, \mathbf{E}_{r_0}\}$ by a scattering matrix **S**, such that

$$\begin{bmatrix} \mathbf{E}_l \\ \mathbf{E}_r \end{bmatrix} = \begin{bmatrix} S_2 & S_3 \\ S_4 & S_1 \end{bmatrix} \begin{bmatrix} \mathbf{E}_{l_0} \\ \mathbf{E}_{r_0} \end{bmatrix} \frac{\exp(-ikr_0)}{ikr_0} \tag{A2}$$

where l and r refer to the electric fields directions parallel and perpendicular, respectively, to a horizontal scattering plane, r_0 is the distance between detector and scatterer, $k = 2\pi/\lambda$, and $i = (-1)^{1/2}$. In experiments, two kinds of SALS measurement are commonly made: H_v measurement where the scatterer is placed between two crossed linear polarizers and V_v measurement where the polarizers are uncrossed. It has been shown in the small-angle approximation that[38]

$$I_{V_v} = \frac{I_0}{k^2 {r_0}^2} |S_1 \sin^2\varphi + S_2 \cos^2\varphi + (S_3 - S_4) \sin\varphi \cos\varphi|^2 \tag{A3}$$

and

$$I_{H_v} = \frac{I_0}{k^2 {r_0}^2} |S_3 \sin^2\varphi - S_4 \cos^2\varphi + (S_2 - S_1) \sin\varphi \cos\varphi|^2 \tag{A4}$$

where I_0 is the incident light intensity and φ is the azimuthal angle. For the spherical symmetric scatterer, Van de Hulst[37] showed that $S_3 = S_4 = 0$ for any scattered angle, and $S_1 \neq S_2$ for $\theta > 0$. Equations A3 and A4 then become

$$I_{V_v} = \frac{I_0}{k^2 {r_0}^2} |S_1 \sin^2\varphi + S_2 \cos^2\varphi|^2 \tag{A5}$$

and

$$I_{H_v} = \frac{I_0}{k^2 r_0^{\,2}} |S_2 - S_1|^2 \sin^2 2\varphi \tag{A6}$$

The light scattered by a homogeneous, spherical symmetric scatterer through a scattered angle θ is completely described by the components S_1 and S_2. Equations A5 and A6 predict the V_v scattering pattern with 2-fold symmetry and the H_v scattering pattern with 4-fold symmetry, respectively.

Meeten and Navard have be given the expressions for S_1 and S_2 using the Rayleigh−Gans−Debye (RGD) light-scattering approximation.[38−40] The conditions defining the validity range of the RGD approximation are generally stated as $|\mu - 1| \ll 1$, $2ka_0|\mu - 1| \ll 1$, and $ka_0 > 1$, where a_0 is the spherical radius and μ is the relative mean refractive index.[37] If the birefringent sphere is surrounded by an isotropic medium of refractive index m_1, then μ is defined by $\mu = (m_r + 2m_t)/3m_1$ and the birefringence index is defined by $\Delta\mu = (m_r - m_t)/m_1$, where m_r and m_t are the radial and tangential refractive indices of the sphere, respectively. The expressions for S_1 and S_2 in the RGD approximation are then[40]

$$S_1 = \frac{2ik^3a^3}{3u^3}\{3(\mu - 1)(\sin u - u\cos u) + \Delta\mu[u\cos u - 4\sin u + 3Si(u)]\} \tag{A7}$$

$$S_2 = \frac{2ik^3a^3}{3u^3}\{3(\mu - 1)(\sin u - u\cos u)\cos\theta - \Delta\mu[1 + \cos^2(\theta/2)][u\cos u - 4\sin u Si(u)]\} \tag{A8}$$

where the parameter u is defined by $u = qa_0$ and $Si(u)$ is defined by

$$Si(u) = \int_0^u \frac{\sin x}{x}\,dx \tag{A9}$$

The second term in eqs A7 and A8 will be zero for the case where $\Delta\mu = 0$, and the equations will reduce to the familiar equations for the light scattered by an isotropic sphere.

Appendix B

The assumption of scale invariance implies that the pair-correlation function of the fractal aggregate in a d-dimensional space can be written as[20−22]

$$g(r) - 1 = \frac{D_f}{4\pi\rho(a_0)^{D_f}} r^{D_f-3} h\left(\frac{r}{\xi}\right) \quad \text{with } r > a_0 \tag{B1}$$

where ρ is the number density of the particles in the system and $h(r/\xi)$ is a cutoff function. $h(r/\xi)$ is close to unity for $r \ll \mathrm{l}\ \xi$ (where ξ is the characteristic upper cutoff size of the aggregate) and rapidly drops to zero for $r > \xi$. The form of cutoff function has been discussed by many authors.[20,41,42] The most used cutoff is the exponential form $h(r/\xi) = \mathrm{e}^{-r/\xi}$ where the cutoff size is related to the radius of gyration by $\xi^2 = 2R_g^2/[D_f(D_f + 1)]$.[42] The structure factor $S(q)$ and the pair-correlation function $g(r)$ are Fourier transform pairs and can be expressed as follows:[20]

$$S(q) = 1 + \rho\int_0^\infty \frac{[g(r) - 1]\sin(qr)}{qr} 4\pi r^2\,dr = 1 + \frac{D_f\Gamma(D_f - 1)}{(qa_0)^{D_f}(1 + 1/q^2\xi^2)^{(D_f-1)/2}} \sin[(D_f - 1)\tan^{-1}(q\xi)] \tag{B2}$$

where $\Gamma(x)$ is the gamma function.

Appendix C

Using a simplified geometry to represent the scatterer, Dubois et al.[43] have given expressions for the scattering by the randomly dispersed sphere doublets. They approached the problem in which the sphere doublet is approximated by two interpenetrated spheres scattering independently. On the basis of this model, the form factor of the sphere doublet can be written as[43]

$$P^d_{V_v}(q) = A^{-1}|S_2\cos^2\varphi + S_1\sin^2\varphi|^2\left\{\cos^2\left[\frac{k}{2}(R_A - R_B)\right]\right\} \tag{C1}$$

and

$$P^d_{H_v}(q) = A^{-1}|S_2 - S_1|^2\sin^2 2\varphi\left\{\cos^2\left[\frac{k}{2}(R_A - R_B)\right]\right\} \tag{C2}$$

where the $R_A - R_B$ is the optical path difference from the origins A and B of the two spheres to a point in the scattering plane, and A is the cross-sectional area in the case of the sphere doublet. The term in brackets is from the interference between the two spheres. As seen form Figure 8b, the sphere doublet is more like overlapping spheres. We can also define an overlapping parameter $F(t) = a_0/a_r(t)$. For two spheres in contact, $F = 1$. If the coarsening of two contact spheres, $F < 1$. The cross-sectional area of the two interpenetrated spheres is equal to $A = 2\pi a_r^2 - 2a_r^2 \arccos F + 2a_r^2F\sqrt{1-F^2}$. From the phenomenological point of view, the arrangement of aggregating particles in fractal clusters can be qualitatively regarded as the sphere doublets oriented with random dispersion in system. The form factor can be written as[43]

$$P^d_{V_v}(q) = |S_2\cos^2\varphi + S_1\sin^2\varphi|^2\frac{{}^1/_2 + J_0(2ka_r F\sin\theta)}{a_r^{\,2}(2\pi - 3\arccos F + 2F\sqrt{1 - F^2})} \tag{C3}$$

$$P^d_{H_v}(q) = |S_2 - S_1|^2\sin^2 2\varphi\frac{{}^1/_2 + J_0(2ka_r F\sin\theta)}{a_r^{\,2}(2\pi - 3\arccos F + 2F\sqrt{1 - F^2})} \tag{C4}$$

where J_0 is the zeroth-order Bessel function.

References and Notes

(1) Stauffer, D.; Coniglio, A.; Adam, M. *Adv. Polym. Sci.* **1982**, *44*, 105.
(2) Coniglio, A.; Stanley, H. E.; Klein, W. *Phys. Rev. Lett.* **1977**, *42*, 518.
(3) Zallen, R. *The Physical of Amorphous Solids*; John Wiley & Sons: New York, 1998.
(4) Keller, A. *Faraday Discuss.* **1995**, *101*, 1.
(5) Te Nijenhuis, K. *Thermoreversible Networks*; Springer: New York, 1997.

(6) Guenet, J. M. *Thermoreversible Gelation of Polymer and Biopolymer*; Academic Press: London, 1992.
(7) Chou, C. M.; Hong, P. D. *Macromolecules* **2003**, *36*, 7331.
(8) Schätzel, K.; Ackerson, B. J. *Phys. Rev. Lett.* **1992**, *68*, 337.
(9) Carpineti, M.; Giglio, M. *Phys. Rev. Lett.* **1992**, *68*, 3327.
(10) Takenaka, M.; Izumitani, T.; Hashimoto, T. *J. Chem. Phys.* **1990**, *92*, 4566.
(11) Bates, F. S.; Wiltzius, P. *J. Chem. Phys.* **1989**, *91*, 3258.
(12) Monno, M.; Palma, M. U. *Phys. Rev. Lett.* **1997**, *79*, 4286.
(13) Takeshita, H.; Kanaya, T.; Nishidam, K.; Kaji, K. *Macromolecules* **1999**, *32*, 7815.
(14) Stein, R. S.; Rhodes, M. B. *J. Appl. Phys.* **1960**, *31*, 1873.
(15) Rhodes, M. B.; Stein, R. S. *J. Polym. Sci., Part A2* **1969**, *7*, 1538.
(16) Hong, P. D.; Chou, C. M. *Macromolecules* **2000**, *33*, 9673.
(17) Hong, P. D.; Chou, C. M. *Polymer* **2000**, *41*, 8311.
(18) Meeten, G. H. *Optical Properties of Polymers*; Elsevier: London, 1986.
(19) Forrest, S. R.; Witten, T. A. *J. Phys. A* **1979**, *12*, L109.
(20) Stanley, H. E.; Ostrowski, N. *On Growth and Form: Fractal and Non-Fractal Patterns in Physics*; Nijhoff: Dordrecht, 1986.
(21) Family, F.; Landau, D. P. *Kinetics of Aggregation and Gelation*; North-Holland: Amsterdam, 1984.
(22) Bushell, G. C.; Yan, Y. D.; Woodfield, D.; Raper, J.; Amal, R. *Adv. Colloid Interface Sci.* **2002**, *95*, 1.
(23) Dimon, P.; Sinha, S. K.; Weitz, D. A.; Safinya, C. R.; Smith, G. S.; Varady, W. A.; Lindsay, H. M. *Phys. Rev. Lett.* **1986**, *57*, 595.
(24) Brown, W. *Light Scattering: Principles and Development*; Clarendon Press: Oxford, 1996.
(25) Lattuada, M.; Wu, H.; Hasmy, A.; Morbidelli, M. *Langmuir* **2003**, *19*, 6312.
(26) Hasmy, A.; Foret, M.; Pelous, J.; Jullien, R. *Phys. Rev. B* **1993**, *48*, 9345.
(27) Oh, C.; Sorensen, C. M. *Phys. Rev. E* **1998**, *57*, 784.
(28) Yang, G.; Biswas, P. *J. Colloid Interface Sci.* **1999**, *211*, 142.
(29) Limary, R.; Green, P. F. *Phys. Rev. E* **2002**, *66*, 021601.
(30) Yao, J. H.; Elder, K. R.; Guo, H.; Grant, M. *Phys. Rev. B* **1993**, *47*, 14110.
(31) Nikolayve, V. S.; Beysens, D.; Guenoun, P. *Phys. Rev. Lett.* **1996**, *76*, 3144.
(32) Rosenfeld, G.; Morgenstern, K.; Esser, M.; Comsa, G. *Appl. Phys. A* **1999**, *69*, 489.
(33) Lifshitz, I. M.; Slyozov, V. V. *J. Phys. Chem. Solids* **1961**, *19*, 35.
(34) Wagner, C. *Z. Electrochem.* **1961**, *65*, 581.
(35) Binder, K. *Phys. Rev. A* **1984**, *29*, 341.
(36) Olmsted, P. D.; Poon, W. C. K.; Mcleish, T. C. B.; Terrill, N. J.; Ryan, A. J. *Phys. Rev. Lett.* **1998**, *81*, 373.
(37) Van de Hulst, H. C. *Light Scattering by Small Particles*; John Wiley & Sons: New York, 1975.
(38) Meeten, G. H. *Opt. Acta* **1982**, *26*, 759.
(39) Meeten, G. H.; Navard, P. *J. Polym. Sci., Part B: Polym. Phys.* **1984**, *22*, 2159.
(40) Meeten, G. H.; Navard, P. *J. Polym. Sci., Part B: Polym. Phys.* **1989**, *27*, 2023.
(41) Cai, J.; Lu, N.; Sorensen, C. M. *J. Colloid Interface Sci.* **1995**, *171*, 470.
(42) Sorensen, C. M.; Wang, G. M. *Phys. Rev. E* **1999**, *60*, 7143.
(43) Dubois, J.; Fyen, W.; Rusu, D.; Peuvrel-Disdier, E.; Navard, P. *J. Polym. Sci., Part B: Polym. Phys.* **1998**, *36*, 2005.

MA049361F